Quantitative analysis of a III-V tapered horn-shaped metal-clad nano-cavity as an on-chip light source

Sukmo Koo, Radwanul Hasan Siddique, and Hyuck Choo

Citation: AIP Advances **7**, 075017 (2017); doi: 10.1063/1.4995590
View online: http://dx.doi.org/10.1063/1.4995590
View Table of Contents: http://aip.scitation.org/toc/adv/7/7
Published by the American Institute of Physics

Quantitative analysis of a III-V tapered horn-shaped metal-clad nano-cavity as an on-chip light source

Sukmo Koo,[1] Radwanul Hasan Siddique,[1] and Hyuck Choo[1,2,a]
[1]*Moore Laboratory, Department of Medical Engineering, California Institute of Technology, Pasadena, CA 91125, USA*
[2]*Moore Laboratory, Department of Electrical Engineering, California Institute of Technology, Pasadena, CA 91125, USA*

(Received 9 March 2017; accepted 10 July 2017; published online 31 July 2017)

A *horn-shaped* metal-clad InGaAsP nano-cavity with sloped sidewalls is proposed as a platform for nanoscale light sources. The nano-cavity's physical dimensions are 350 × 350 × 350 nm^3, and its mode volume is 0.5 $(\lambda_0/n)^3$. In our numerical simulations and quantitative analysis, we have shown that the sloped sidewalls reduce metallic absorption and improve resonant mode confinement; and adjusting their slope from 0 to 16° increased the Q factor from 150 to 900 and laser modulation 3dB bandwidth from 4.3 to 36 GHz. The lasing threshold current was expected to be 35 μA at 16°. In a simulated feasibility study, we demonstrate 60 Gbps modulated laser signal (5 fJ/bit), producing 20 μW output power at the 1.5 μm wavelength with injection current 100 μA, as an implementation of horn-shaped nano-cavity platform to the low power and ultra-fast on-chip nano-laser. [http://dx.doi.org/10.1063/1.4995590]

The physical size of an on-chip light-source's resonant cavity should be small enough to promote easy coupling of light into an integrated waveguide. When compared to conventional dielectric resonators,[1–6] using a metallic cavity can enhance the light confinement and, as a result, metal-based plasmonic resonators produce extremely small laser modal sizes on the order of $10^{-3} \sim 10^{-1}$ $(\lambda_0/n)^3$.[6–10] However, the Q factors of the plasmonic resonators are very small, ranging between 10-100, because the optical mode largely overlaps with the metallic region, making them unsuitable for laser applications.[7–9]

Using the metal-clad cavity[6,11–16] is an alternative way to reduce modal overlap with the metal shielding and thereby the metallic loss in plasmonic resonators. Their advantages as a platform for on-chip nano-laser have been reported previously:[11,12] high Q (~1,000) factors and small modal volumes ~sub-$(\lambda_0/n)^3$, as well as the feasibility of high directional coupling efficiency (>90%) to the integrated waveguides. Their Q factors and Purcell enhancement have been maximized by optimizing the thickness of the dielectric cladding layer and the position of the gain medium.[11,12] Optimizing the cavity design for high Q and Purcell factor, and direct analysis of the relation between the design structure and the laser operation speed, threshold pump are highly desirable to maximize the performance as on-chip laser.

In this paper, given the main sources of leakage observed in metal-clad cavities are the cavity opening in the bottom and the metallic absorption, a *horn shaped* metal-clad optical cavity with a sidewall slope (α) is proposed to reduce leakage and optimize the resonator properties such as the Q factor, modal volume and Purcell enhancement factor. III-V InGaAsP was chosen for the gain material, which generates spontaneous emission at a wavelength range between 1.3 μm to 1.67 μm.[13] The inverted horn-shaped cladding shifts the mode horizontally to the wider region in the upper part

[a]Corresponding author: hchoo@caltech.edu

of the cavity reducing the leakage or radiation and absorption losses simultaneously. Based on this horn-shaped cavity, we designed a laser and used the laser rate equations to perform quantitative analysis to predict two important performance metrics: modulation speed and threshold pump (current). The Q factor, modal volume, and Purcell enhancement factor were optimized to find the minimum threshold current and modulation speed saturation. We also performed a large signal analysis to numerically generate an eye diagram by modulating the laser power and injection.

The nano-horn metal-clad resonator is illustrated in Fig. 1(a). The resonator consists of a III-V InGaAsP cavity whose volume is $350 \times 350 \times 350$ nm^3 and a current-conducting InP post. Both components are shielded inside SiO_2 cladding and an Ag top layer with *sloped sidewalls* to suppress the leaky optical mode.[11,12,14] Detailed structural parameters are described in Fig. 1(a). A SiO_2 spacer is placed underneath the cavity to insulate the InP substrate from the metal. To calculate the quality factor of this structure, a Finite Difference Time Domain analysis was performed using Lumerical Solutions, a commercially available software.[17] Since the change of the electromagnetic field is abrupt inside the metal, we used a minimum grid size of 4 nm in this region (about one sixth of the skin depth, which is approximately 25 nm), while a grid size of 12 nm is used outside the resonator. As it can be seen from Fig. 1(b), using these mesh conditions yielded smooth and sufficiently detailed field patterns that showed the rapidly changing field distribution. Refractive indices appropriate for the operation wavelength regime of $\lambda = 1.2 \sim 1.7$ μm were defined as 3.4 for InGaAsP, 3.16 for InP, 1.45 for SiO_2, and the dispersive relation found in reference 18 for Ag. The broadband ($\lambda = 1.2 \sim 1.7$ μm) dipole point source was designed to be placed inside the InGaAsP cavity to ensure the coupling of the fundamental resonance mode, as shown in Fig. 1(b). Since we focused on evaluating the use of this resonator for light-source implementation, we calculated the Q factor, resonance wavelength λ_0, energy-overlap factor in the active InGaAsP region Γ, quantum efficiency η, and mode volume V_{norm}.

The Q factor can be decomposed into the absorption and radiation components ($Q^{-1} = Q_{abs}^{-1} + Q_{rad}^{-1}$).[9,10] This can be observed in Fig. 1(b). The strong current density distribution at the metallic layer near the cavity indicates the energy absorption Q_{abs} due to the spatial spread of the mode. Q_{rad} is indicated by the leaky electric field under the cavity that causes energy to radiate into the InP substrate through the dielectric passage. In our proposed design, the wider cladding region near the cavity reduces optical absorption and the narrowing passage near the bottom enhances the vertical confinement.[11] Hence, introducing an additional design parameter α for the tapering angle provides another leverage to control Q_{abs} and Q_{rad}, which will lead to further enhancement of the overall quality factor Q.

To study the role of the α, the position of the gain medium ($h_{top} = 50$ nm, $h_{bot} = 400$ nm) and the bottom cladding layer thickness ($a_{bot} = 20$ nm) were fixed. When the tapering angle α was increased,

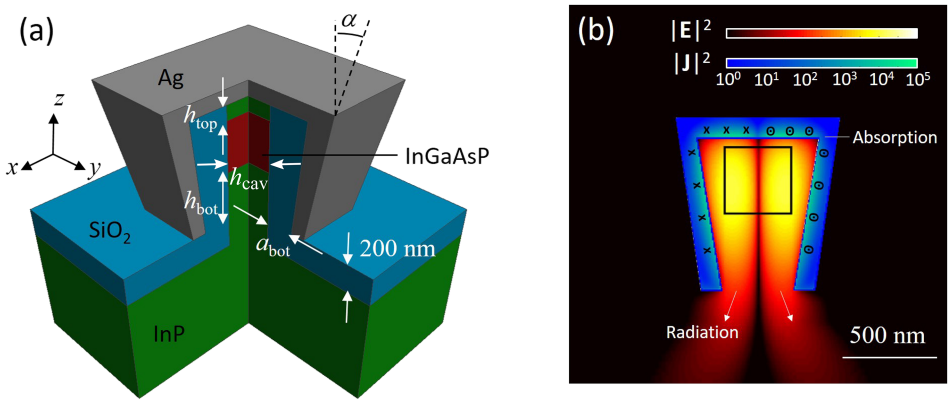

FIG. 1. (a) Schematics of the proposed horn-shaped metal-clad resonator. InGaAsP cubic cavity ($V = 350 \times 350 \times 350$ nm^3) is connected with InP posts with consistent cross section heights h_{top} and h_{bot}, surrounded by slopped (angle: α) SiO_2 cladding (a_{bot}: thicknesses at the bottom) and a Ag top layer (100 nm thickness). The thickness of the SiO_2 spacer is 200 nm. (b) yz-plane cross section view of the electric field ($|\mathbf{E}|^2$) and current ($|\mathbf{J}|^2$ in Ag layer, black symbols denote the direction) intensity (A.U.) pattern of the resonance mode ($\lambda_0 = 1.43$ μm) when $h_{top} = 50$ nm, $h_{bot} = 400$ nm, $a_{bot} = 20$ nm, and $\alpha = 9°$. The black box depicts the InGaAsP cavity region.

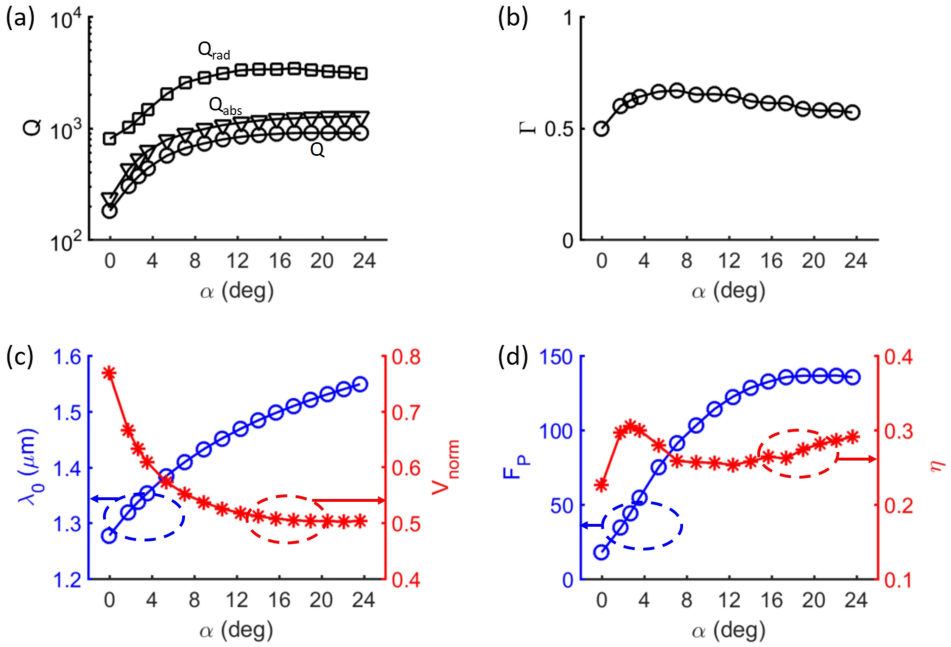

FIG. 2. The properties of the horn-shaped metallic-clad cavity for different slope angles α (a_{bot} = 20 nm). (a) Quality factors (Q: total, Q_{abs}: absorption, Q_{rad}: radiation), (b) overlap factor (Γ), (c) resonance wavelength (λ_0), normalized modal volume (V_{norm}), (d) Purcell factor (F_P) and quantum efficiency (η) are plotted, respectively.

Q_{rad} and Q_{abs} increase due to the higher confinement of energy in the cavity as shown in Fig. 2(a). The position of the resonance mode moves upward toward the wider cladding region in the cavity and reduces the leakage as well as metallic absorption. The overlap factor, Γ, in Fig. 2(b) is also increased for larger α (< 8°) due to this upward shift in the resonance mode position. Γ was shown to decrease slightly for α > 8° because the mode spreads into a larger cladding region. As the percentage of the energy in the high index cavity area increases for larger α, the resonance wavelength increases with the decreasing normalized modal volume given by the following relation, a widely used formula for both dielectric and metallic cavities:[1,19–21]

$$V_{norm} = (n_{InGaAsP}/\lambda_0)^3 \int W_E dV / \max\{W_E\}$$

where W_E is electric energy density as shown in Fig. 2(c).[1,22] The quantum efficiency ($\eta = Q/Q_{rad}$) and Purcell factor [$F_P = 3/(4\pi^2) \times (Q/V_{norm})$], critical factors in determining the performance of the laser, LED, and detector,[7] have been plotted for different α in Fig. 2(d). η reaches a maximum near $\alpha = 3°$ because the Q_{abs} increases faster than Q_{rad} up to $\alpha \sim 4°$. In contrast, F_P ($\sim Q/V_{norm}$) increased with α up to 16° resulting from its dependency on Q and V_{norm}. Increasing α increases the quality factor Q and Purcell factor F_P, and this in turn enhances the spontaneous emission rate[8,9] and naturally improves the performance of nano LEDs and lasers. It is noted that the F_P is not directly related to the enhancement of the spontaneous emission rate because of the non-ideal spontaneous emission coupling to the desired resonance mode.[16,23] In this case, the spontaneous emission coupling factor β has to be considered; when $\beta = 0.1$ and $F_P = 135$ ($\alpha = 16°$) for example, the effective spontaneous rate enhancement becomes $\beta F_P = 13.5$.[23]

In order to investigate the underlying mechanism that pushes the mode towards the wider cladding region inside the cavity, we focused on coupling between the surface plasmon polaritons on two dielectric-metal interfaces separated by the dimension of the cubic gain medium h_{cav} plus 2×a_{bot} and have developed an analytical dispersion expression that illustrates how the effective index of the mode depends on the tapering angle α. The thickness of the SiO_2 (ε_s = 2.1) layer that varies along the Ag surface due to the tapering is defined as h_{cav}tanα. The relative permittivity of the fixed part of the SiO_2 between the InGaAsP gain medium and the medium itself whose cross-sectional dimensions are 2×a_{bot} and h_{cav} can be calculated from Maxwell-Garnett model, i.e. ε_r = 10.6. If we

consider the symmetric mode of coupled surface plasmon polaritons and assume the magnetic field component maintains the sign across the dielectric layers, the dispersion relation for this mode can be described as:[24]

$$\frac{\varepsilon_m k_s + \varepsilon_s k_m}{\varepsilon_m k_s - \varepsilon_s k_m} e^{k_s * 2h_{cav} \tan\alpha} = \frac{\varepsilon_r k_s - \varepsilon_s k_r \tanh\left(k_r\left(\frac{h_{cav}}{2} + a_{bot}\right)\right)}{\varepsilon_r k_s + \varepsilon_s k_r \tanh\left(k_r\left(\frac{h_{cav}}{2} + a_{bot}\right)\right)},$$
$$k_m = \sqrt{\beta^2 - \varepsilon_m k_0^2},$$
$$k_s = \sqrt{\beta^2 - \varepsilon_s k_0^2},$$
$$k_r = \sqrt{\beta^2 - \varepsilon_r k_0^2}, \quad (1)$$

where, ε_m is the relative permittivity of the metal (Ag), β is the propagation constant, and k_0 is the wave number in vacuum. Eq. (1) allows us to numerically analyze the dependence of the modal effective index ($n_{eff} = \beta/k_0$) on the tapering angle α, and it shows that n_{eff} increases as α increases for the wavelength range of interest (λ = 1.3 – 1.67 μm), thereby forcing the resonant mode to shift towards the wider cladding region with an increasing tapering angle.

To further investigate the use of our structure in practical applications, a quantitative study of the structure in terms of threshold current, power consumption, and modulation speed was performed. To calculate the power consumption and operational speed of the proposed light source platform, the well-known rate equations[8–10] relating the pumping rate p (= I/q in the case of ideal current injection, where I is current and q is electron charge) and the number of photons in the laser mode S shown below were utilized,

$$\frac{dN}{dt} = p - AN - \beta\Gamma AS(N - n_0),$$
$$\frac{dS}{dt} = \beta AN + \beta\Gamma AS(N - n_0) - \gamma S \quad (2)$$

where N is the excited state population, n_0 (~1.25×10^{18} cm^{-3} × V = 5.36×10^4 for the InGaAsP cavity) is the excited state population at transparency, A (= $F_P A_i$, A_i is the natural spontaneous emission rate ~ 3×10^7 s^{-1} for InGaAsP) is the spontaneous emission rate, β is the spontaneous emission coupling factor[16,23] that is assumed to be 0.1, and γ (= ω_0/Q) is the total cavity mode loss rate.

Using Eq. (1), the output power P_{out} [= $\eta \cdot (hc/\lambda_0) \cdot (n_{InGaAsP}/\lambda_0)^3 V_{norm} \cdot \gamma S$] for different pump rates p at steady state conditions ($d/dt \to 0$ in the limit of very low ($p \to 0$) and high ($p \to \infty$) pump rates) described below were used to investigate distinct linear responses.[8–10]

$$P_{out}|_{p\to 0} = \frac{hc\lambda_0{}^2}{n_{InGaAsP}^3} \frac{\eta V_{norm}\gamma}{\Gamma} \times \frac{p}{p_{th}}$$
$$P_{out}|_{p\to\infty} = \frac{hc\lambda_0{}^2}{n_{InGaAsP}^3} \frac{\eta V_{norm}}{\Gamma} \times [p - (1-\beta)An_\infty] \quad (3)$$

where

$$n_\infty = n_0 + \gamma/(\beta\Gamma A) \text{ and } p_{th} = An_0(1 - \beta) + \gamma/(\beta\Gamma).$$

From Eqs. (1), (2) and as well as the parameters (Q, λ_0, Γ, η and V_{norm}) extracted from the FDTD simulations, the results of P_{out} and N are plotted in Fig. 3(a) for the proposed structure and show similar properties as previously reported lasers.[8–10] The required threshold current calculated from $I_{th} = qp_{th}$ is plotted in Fig. 3(c). The minimum I_{th} of 20 μA or 16 kA/cm^2 is achieved when α is near 3° because Q (= ω_0/γ) and F_P (= A/A_i) increase as α becomes larger and this in turn decreases I_{th} (= $q\gamma/(\beta\Gamma) + qAn_0(1-\beta)$). It is noted that for $\alpha > 3°$, the non-ideal spontaneous coupling increases the I_{th} with F_P. As can be seen from the previous expression, I_{th} has a little dependency on η in Fig. 2(d) but changes for different β values as shown in Fig. 3(c). To examine the power efficiency for different slope angles, injection currents of I (= 8 μA < I_{th}) and I (= 80 μA > I_{th}) were implemented

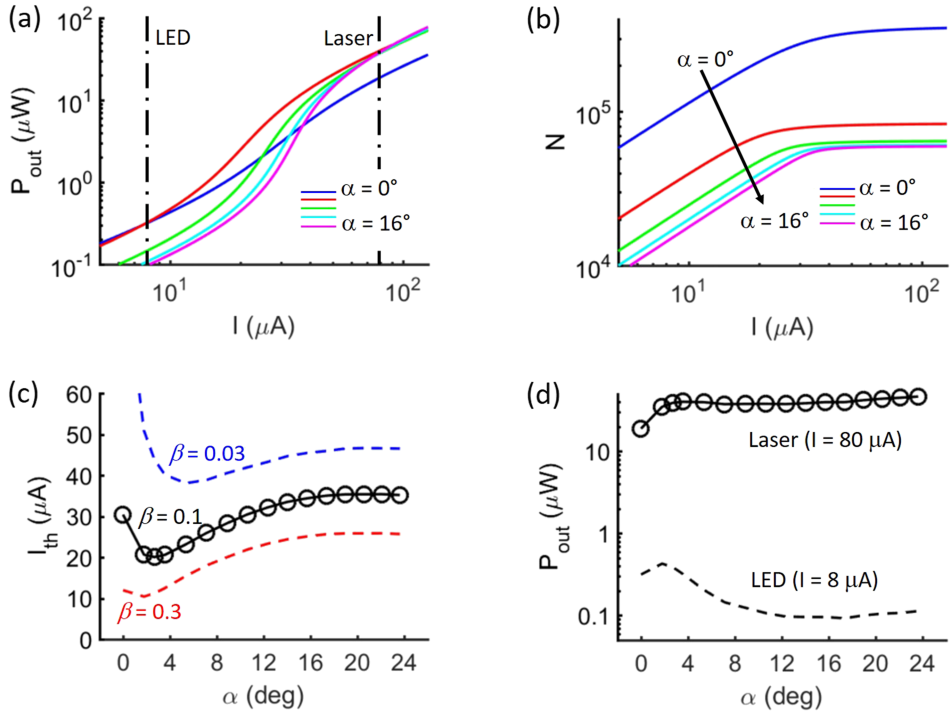

FIG. 3. (a) Laser output power P_{out} and (b) excited state population N for different injection currents (pump rate) calculated from Eq. (2) with $\beta = 0.1$. (c) Calculated threshold current I_{th} (= qp_{th}) for different α ($\beta = 0.03$, 0.1 and 0.3). (d) P_{out} for the laser ($I = 80$ μA) and LED ($I = 8$ μA) of the proposed cavity for different slope α ($\beta = 0.1$).

to compare the output power of the LED and laser as shown in Fig. 3(d). While the laser output power does not show significant dependence on α after reaching saturation at 3°, the LED output power reaches a maximum at 3°, decreases up to 12°, and then stabilizes for larger angles.

We now calculate frequency response from Eq. (1) by substituting $d/dt \rightarrow i\omega$, $S \rightarrow S_0 + s(\omega)e^{i\omega t}$, $p \rightarrow p_0 + p(\omega)e^{i\omega t}$ and $N \rightarrow N_0 + n(\omega)e^{i\omega t}$ for the small signal frequency response where S_0, p_0, and N_0 are the steady state photon number, pumping rate and excited state population, respectively. First-ordering Eq. (1) and utilizing the small signal components $s(\omega)$, $p(\omega)$ and $n(\omega)$ allows the frequency response function $\Theta(\omega) = s(\omega)/p(\omega)$ of the system to be derived as

$$\Theta(\omega) = \frac{A\beta(1 - \Gamma S_0)}{[i\omega + \gamma - A\beta\Gamma(N_0 - n_0)][i\omega + A(1 + \beta\Gamma S_0)] + A^2\beta^2\Gamma(N_0 - n_0)(1 - \Gamma S_0)} \quad (4)$$

The frequency response of Eq. (3) and 3dB bandwidth f_{3dB} are plotted in Fig. 4(a) and (b). The operation frequency of the laser increased from 4.3 to 36 GHz as α changed from 0° to 8° and then saturated for $\alpha > 8°$. Similarly, the operating frequency of the LED increased from 0.15 to 1 GHz for α up to 16° before reaching saturation. As shown, the modulation speed for the laser ($I = 80$ μA) is faster than the LED ($I = 8$ μA).

To demonstrate the high speed modulation, a large signal analysis was used to calculate the transient response of the output power P_{out} in Eq. (1) for the nanocavity with optimized slope ($\alpha = 4°$), minimized $I_{th} = 20$ μA, and almost saturated $f_{3dB} = 29$ GHz. A continuous wave input signal made of 60 Gbps nonreturn-to-zero (NRZ) pseudorandom 2^7 - 1 bit sequence (PRBS) was injected into the cavity with an assumed transit time of 10 ps from entering from the metal contact to the gain medium, as shown in the blue line in Fig. 4(c).[2] Using Eq. (1), the output signal of the laser and its eye diagram were obtained and plotted in Fig. 4(c) and (d). An open eye pattern is clearly shown in Fig. 4(d). The calculated eye SNR and jitter time are 6.2 dB and 0.8 ps. Assuming the voltage 3V across the junction,[25] the estimated power consumption is 5 fJ/bit which is under the criteria of required energy per bit (50 fJ/bit) to compete electrical interconnects.[25]

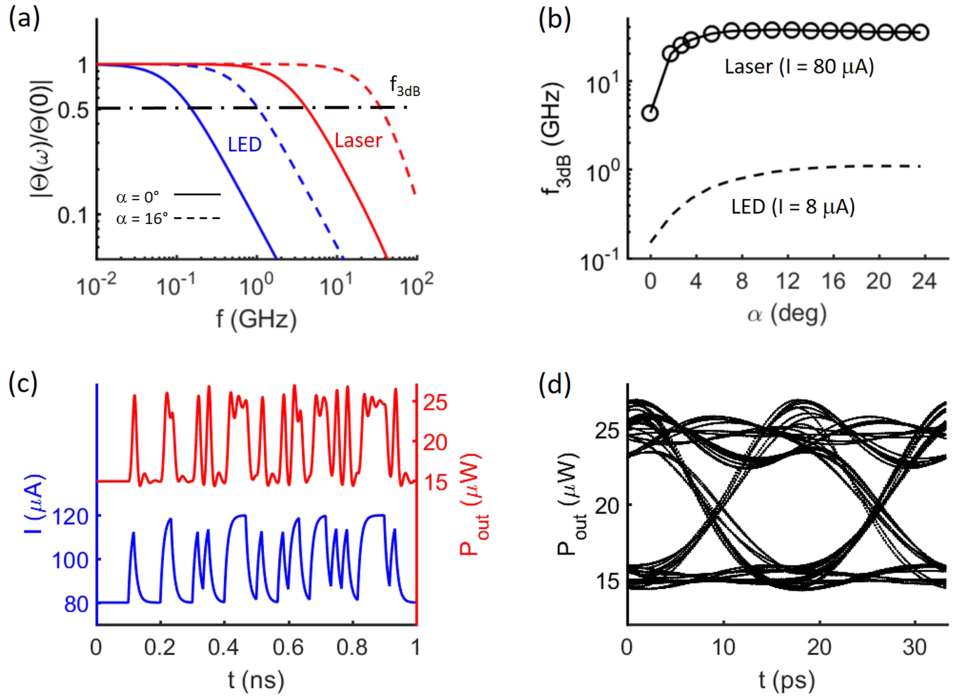

FIG. 4. (a) Frequency response function at defined slopes ($\alpha = 0°$ and 16°) and current injections for the laser ($I = 80$ μA) and LED ($I = 8$ μA). (b) f_{3dB} as a function of slope, α. (c) Injected current (blue, assuming transit time 10 ps) based on the (2^7-1) PRBS, 60 Gbps modulation and output laser signal (red) calculated from Eq. (1) when $\alpha = 4°$. (d) Simulated eye diagram for the output optical laser power from (c). All calculations assumed $\beta = 0.1$.

To summarize, a proposed *horn-shaped* metal clad cavity was determined to have significantly improved properties as a platform for nanoscale light sources. The inverted sloped geometry of the metal-clad cavity pushes the resonance mode into the upper part of the cavity, increasing the energy confinement in the dielectric region and reducing radiation and absorption losses in the metal layer. By increasing the cladding slope angle from 0 to 16°, the Q and Purcell factors increased by a factor of 18 from 50 to 900 and by a factor of 7.5 from 18 to 135, respectively. From the laser rate equation, the laser threshold injection current was shown to reach a minimum of $I_{th} = 20$ μA at $\alpha = 4°$. The laser modulation speed increased as the slope angle increased from 0 to 8° and saturated at $f_{3dB} = 36$ GHz for larger angles. For the LED, f_{3dB} increased from 0.15 to 1 GHz and saturated for α larger than 16°. Operating at $I_{th} = 20$ μA and $f_{3dB} = 29$ GHz, the feasibility of a 60-Gbit-modulated laser (with α set at the optimized value of 4°) was demonstrated by an open eye diagram with a good signal-to-noise ratio and small jitter. Using a III-V InGaAsP active region in simulation, our approach is valid for the wavelength range of the InGaAsP photoluminescence spectrum, which ranges from 1.3 to 1.67 μm.[13] This approach and analysis can serve as a design guideline toward implementing ultra-compact, ultra-fast, and cost-efficient on-chip metal-clad nanoscale lasers.

ACKNOWLEDGMENTS

This work has been supported by the Moore Foundation, Intellectual Ventures, and the Heritage Medical Research Institute. We appreciate Zheng Li for helpful discussions and inspiring the project.

[1] R. Coccioli, M. Boroditsky, K. W. Kim, Y. Rahmat-Samii, and E. Yablonovitch, "Smallest possible electromagnetic mode volume in a dielectric cavity," IEE P-Optoelectron. **145**, 391–397 (1998).
[2] M. Radziunas, A. Glitzky, U. Bandelow, M. Wolfrum, U. Troppenz, J. Kreissl, and W. Rehbein, "Improving the modulation bandwidth in semiconductor lasers by passive feedback," IEEE J. Sel. Top. Quantum Electron. **13**, 136–142 (2007).
[3] U. Bandelow, R. Hünlich, and T. Koprucki, "Simulation of static and dynamic properties of edge-emitting multiple-quantum-well lasers," IEEE J. Sel. Topics Quantum Electron. **9**, 798–806 (2003).

[4] J. Petykiewicz, D. Nam, D. S. Sukhdeo, S. Gupta, S. Buckley, A. Y. Piggott, J. Vučković, and K. C. Saraswat, "Direct bandgap light emission from strained Germanium nanowires coupled with high-Q nanophotonic cavities," Nano Lett. **16**, 2168–2173 (2016).
[5] K. Takeda, T. Sato, A. Shinya, K. Nozaki, W. Kobayashi, H. Taniyama, M. Notomi, K. Hasebe, T. Kakitsuka, and S. Matsuo, "Few-fJ/bit data transmissions using directly modulated lambda-scale embedded active region photonic-crystal lasers," Nat. Photonics **7**, 569–575 (2013).
[6] M. T. Hill and M. C. Gather, "Advances in small lasers," Nat. Photonics **8**, 908–918 (2014).
[7] Z. Li, J.-L. Kou, M. Kim, J. O. Lee, and H. Choo, "Highly efficient and tailorable on-chip metal-insulator-metal plasmonic nanofocusing cavity," ACS Photonics **1**, 944–953 (2014).
[8] N. Li, K. Liu, V. J. Sorger, and D. K. Sadana, "Monolithic III–V on silicon plasmonic nanolaser structure for optical interconnects," Scientific Reports **5**, 14067 (2015).
[9] R.-M. Ma, R. F. Oulton, V. J. Sorger, and X. Zhang, "Plasmon lasers: Coherent light source at molecular scales," Laser Photon. Rev. **7**, 1–21 (2013).
[10] D. A. Genov, R. F. Oulton, G. Bartal, and X. Zhang, "Anomalous spectral scaling of light emission rates in low-dimensional metallic nanostructures," Phys. Rev. B **83**, 245312 (2011).
[11] M.-K. Kim, A. M. Lakhani, and M. C. Wu, "Efficient waveguide-coupling of metal-clad nanolaser cavities," Opt. Express **19**, 23504–23512 (2011).
[12] M.-K. Kim, Z. Li, K. Huang, R. Going, M. C. Wu, and H. Choo, "Engineering of metal-clad optical nanocavity to optimize coupling with integrated waveguides," Opt. Express **21**, 25796–25804 (2013).
[13] Q. Gu, B. Slutsky, F. Vallini, J. S. T. Smalley, M. P. Nezhad, N. C. Frateschi, and Y. Fainman, "Purcell effect in sub-wavelength semiconductor lasers," Opt. Express **21**, 15603–15616 (2013).
[14] M. P. Nezhad, A. Simic, O. Bondarenko, B. Slutsky, A. Mizrahi, L. Feng, V. Lomakin, and Y. Fainman, "Room-temperature subwavelength metallo-dielectric lasers," Nat. Photonics **4**, 395–399 (2010).
[15] I. S. Maksymov, M. Besbes, J. P. Hugonin, J. Yang, A. Beveratos, I. Sagnes, I. Robert-Philip, and P. Lalanne, "Metal-coated nanocylinder cavity for broadband nonclassical light emission," Phys. Rev. Lett. **105**, 180502 (2010).
[16] K. Ding, M. T. Hill, Z. C. Liu, L. J. Yin, P. J. van Veldhoven, and C. Z. Ning, "Record performance of electrical injection subwavelength metallic-cavity semiconductor lasers at room temperature," Opt. Express **21**, 4728–4733 (2013).
[17] A. Taflove and S. C. Hagness, *Computational electromagnetics: the finite-difference time-domain method* (Artech House, 2000).
[18] P. B. Johnson and R. W. Christy, "Optical constants of the noble metals," Phys. Rev. B **6**, 4370–4379 (1972).
[19] P. T. Kristensen and S. Hughes, "Modes and mode volumes of leaky optical cavities and plasmonic nanoresonators," ACS Photonics **1**, 2–10 (2014).
[20] J. T. Robinson, C. Manolatou, L. Chen, and M. Lipson, "Ultrasmall mode volumes in dielectric optical microcavities," Phys. Rev. Lett. **95**, 143901 (2005).
[21] K. Srinivasan, M. Borselli, O. Painter, A. Stintz, and S. Krishna, "Cavity Q, mode volume, and lasing threshold in small diameter AlGaAs microdisks with embedded quantum dots," Opt. Express **14**, 1094–1105 (2006).
[22] R. Ruppin, "Electromagnetic energy density in a dispersive and absorptive material," Physics Letters A **299**, 309–312 (2002).
[23] J. Vuckovic, O. Painter, Y. Xu, A. Yariv, and A. Scherer, "Finite-difference time-domain calculation of the spontaneous emission coupling factor in optical microcavities," IEEE J. Quant. Electron. **35**, 1168–1175 (1999).
[24] S. A. Maier, *Plasmonics: fundamentals and applications*, Springer Science & Business Media (2007).
[25] C.-Y. A. Ni and S. L. Chuang, "Theory of high-speed nanolasers and nanoLEDs," Opt. Express **20**, 16450–16470 (2012).